

<https://doi.org/10.1038/s41528-026-00531-x>

Smart photocapacitive Cu_2SnS_3 quantum dots-based flexible biointerface for retinal-inspired photoelectrical stimulation

Check for updates

Sharadrao A. Vanalakar¹ ✉, Mohammad H. Qureshi² ✉, Mohammad Mohammadiaria³, Sharayu S. Vhanalkar⁴, Jin H. Kim⁵ ✉ & Shashi B. Srivastava^{6,7} ✉

Retinal degeneration, marked by the progressive loss of photoreceptors, is a leading cause of blindness. Photocapacitive biointerfaces provide a prosthesis-style approach to reestablish light-driven neural activity. Here, we present a flexible Cu_2SnS_3 quantum dots/polymer heterojunction (P3HT:PCBM)-based hybrid biointerface that enables wireless photoelectrical stimulation of neurons. The device is forming a stack whose effective capacitance and photocurrent scale with wavelength, emulating retinal spectral sensitivity. When interfaced with neurons, the heterojunction produces red-light-evoked photocurrents (peak ~ 4.5 nA at 8 mW cm^{-2}) and drives measurable changes in both membrane potential and intracellular calcium ($\Delta F/F_0$ increase of $\sim 10\%$). The operation is non-thermal and remains in the capacitive regime, while the hybrid architecture enhances charge separation and interfacial storage compared with single-material layers. These results define a flexible photocapacitive platform that achieves visible/NIR neuromodulation. Validation on hippocampal neurons and future studies on retinal ganglion cells advance this platform toward prosthetic vision applications.

The retina, a thin, light-sensitive tissue located at the back of the eye, plays a crucial role in the visual system. It comprises specialized cells called photoreceptors with rod- and cone-like shapes, which produce bioelectrical impulses by absorbing light rays. These impulses are then decoded by the brain, allowing humans to see. Although the eye is the most important sensory organ in the body, several factors, such as genetic mutations, aging, and certain diseases like Stargardt, retinitis pigmentosa, cone disorders, congenital stationary night blindness and age-related macular degeneration or conditions like diabetic retinopathy, retinal detachment, macular holes, or inflammation of the retina, uveitis, and excessive exposure to UV rays, are responsible for the irretrievable deterioration of photoreceptors, which are medically coined as retinal degeneration (RD)^{1,2}. In the absence of effective intrinsic photoreceptor regeneration, subretinal prosthesis and materials-engineered bioelectronic interfaces have emerged as promising strategies to

improve therapeutic efficacy. Advancements in science and technology have opened up new possibilities for replacing damaged photoreceptors, such as optogenetics, stem cell technology, retinal tissue engineering, and retinal prostheses^{3–8}. The retinal prosthesis is one of the most effective ways to restore lost eyesight, as it offers the potential for visual perception, requires no genetic modification, and is scalable.

However, the prosthesis of the interior body organs is relatively impenetrable compared with that of exterior organs because of the intricacy of the internal system⁹. For example, in the retinal prosthesis, the interface material must undergo several hierarchical discerning developments, such as the reception of visible light, the stimulation of neurons to encode the absorbed photon information into erratic spike frequencies, the coupling of these signals to cells to alter the membrane potential, and more¹⁰. As a result, the material used for the retinal prosthesis must properly address issues such

¹Department of Science, Karmaveer Hire College (Affiliated with Shivaji University, Kolhapur), Gargoti, India. ²Department of Molecular Biology and Genetics, Boğaziçi University, Istanbul, Turkey. ³Independent researcher, Pavia, Italy. ⁴Department of Electrical Engineering, Dr. DY Patil Pratishthan's College of Engineering, Kolhapur, India. ⁵Optoelectronics Convergence Research Center and Department of Materials Science and Engineering, Chonnam National University, Gwangju, Republic of Korea. ⁶Department of Ophthalmology, Henry Ford Health, Detroit, MI, USA. ⁷Department of Physiology, College of Human Medicine, Michigan State University, East Lansing, MI, USA. ✉e-mail: sharadrao.vhanalkar@gmail.com; mohammad.qureshi@bogazici.edu.tr; jinhyeok@chonnam.ac.kr; ssrivass4@hfh.org

as photon response, bioelectrical signal formation, and neurological stimulation, in addition to being biocompatible, non-toxic, and functional. Currently, the photovoltaic substrates as 'biointerfaces' have attracted significant attention¹¹. The photovoltaic material-based retinal neuron stimulation relies on carrier mobility, conduction, and valence-band positions, bending at the edge of biological systems, surface chemistry, and surface states of the material. In conjunction with this, the charge transfer mechanism, which refers to the transport of electrical charges or current to neurons, is crucial for retinal neuron stimulation¹².

Interestingly, capacitors also play a crucial role in this context as a quick charge and rapid discharge tool for delivering precise and rapid electrical pulses to trigger neural activities. Moreover, it is a more suitable device due to its rapid response to current changes¹³. Therefore, materials that have both photovoltaic and capacitive properties could be crucial in stimulating retinal neurons. However, there has not been much research on materials that can stimulate retinal neurons with both characteristics. The device's "smart photocapacitors", which combine the characteristics of a capacitor and a photodetector, enable them to store electrical energy and react to light, which could be used to stimulate neurons. A smart photocapacitor can alter its capacitance in response to incident light, like how the membrane potential of a human eye changes as the light intensity varies^{14–16}.

To date, several photoactive materials, such as silicon (Si), mercury telluride (HgTe), cadmium selenide (CdSe), lead sulfide (PbS), and even lead-based perovskites, have been utilized to convert visible light to bioelectrical stimuli^{17–19}. However, the toxicity of Hg and Pb hinders their real-time in situ application in retinal prosthetic devices. On the other hand, Si has a low absorption coefficient, so a thicker (around 30 μm thick) photoactive layer is needed to construct prosthetic devices. In the milieu of investigation of new bio-interface material with the ability to generate and store charges, we utilized a copper-based ternary metal chalcogenide, Cu_2SnS_3 (CTS). CTS is a less studied semiconductor material than its counterpart, such as CuInS_2 (CIS), and is considered an alternative to rare metal-based multinary chalcogenides such as $\text{Cu}_2\text{InGaSe}_4$ in the photovoltaic industry²⁰. It is one of the most stable members of the Cu-(Zn/In)-Sn/Ga-S semiconductor family and has p-type conductivity, low bandgap energy and a high absorption coefficient²¹. Moreover, the lack of Fermi level pinning, nontoxicity, high charge carrier mobility and earth-abundant constituent elements make it more suitable for the photovoltaic applications^{22,23}.

In the present study, we explore a solution-processed Cu_2SnS_3 quantum dot (CTS QD)- based biointerface architecture to stimulate hippocampal neurons, while ensuring a safe charge injection mechanism in the vicinity of living organisms. The CTS QDs were coupled with (phenyl-C61-butiric acid methyl ester) (PCBM) and poly(3-hexylthiophene) (P3HT) in a bulk heterojunction thin film, and the assemblies were interfaced with the biological medium. P3HT was chosen because of its high biocompatibility, responsivity and tunable charge carrier density²⁴. Meanwhile, the combination of copper-tin-sulphide with a blend of PCBM and P3HT to form a solar cell has not been explored in the literature. However, instead of direct charge transfer, neural activation is based on charge injection via capacitive coupling. Therefore, we explored the ability of CTS to generate electron-hole pairs and their capacitive properties under low-intensity exposure to red light. The smart behavior of CTS, with the ability to charge under low-intensity light exposure, showed effective photoconversion in physiological medium with low cytotoxicity for in vitro hippocampal neuron cultures.

Results

Optimization of the CTS nanoparticles

The solvothermal route was used to prepare CTS QDs using chlorides of copper and zinc along with sodium sulfide as a precursor, and its printable ink was prepared in ethanol (Fig. 1a). The solvothermal deposition time was varied, such as 18, 24, and 30 h, to obtain phase-pure quantum dots. The TEM images show uniform spherical particles of CTS with average diameters in the range of 8–10 nm (Fig. 1b–d) prepared after

30 h of solvothermal treatment. This satisfies the criteria for a quantum dot material with a size of less than 10 nm²⁵. Meanwhile, Fig. 1e shows the X-ray diffractogram of the CTS QDs, where noticeable and broad diffraction peaks were observed (ICDD card No. 89-2877). The absence of distinctive secondary phase peaks in the CTS:30 (CTS prepared in 30 h) sample indicates that the product produced after 30 h was phase pure. The secondary phase peaks with an asterisk (*) suggest that the SnS_2 and Cu-Sn phases, which were observed in samples CTS:18 and CTS:24, could, however, be the result of an incomplete solvothermal reaction. In general, the CTS exhibit a polycrystalline nature with various crystal phases, including cubic, monoclinic, and tetragonal. Therefore, Raman spectroscopy was used to validate the crystal phase, and Fig. 1f shows the Raman spectrum of the CTS powder prepared with 24 and 30 h of solvothermal treatment. The strong peaks at 352 cm^{-1} and the shoulder peak at 290 cm^{-1} for both CTS:24 and CTS:30 samples, which are close to the values reported for CTS thin films, provide evidence that Cu_2SnS_3 exists^{20,26}. The sharp peak located at 352 cm^{-1} proved the presence of a cubic phase in the CTS sample. Meanwhile, weak peaks at 373 cm^{-1} were seen for the CTS:24 sample owing to the presence of SnS_2 impurities. In a neuron photostimulation study, the light absorption and subsequent bioelectric current generation play a vital role; therefore, we have measured the optical absorption capacity of as-prepared CTS in the wavelength range of 500–1000 nm. The optical absorption spans the major visible region, with a peak at a wavelength corresponding to red (Fig. 1g). The CTS nanoparticles exhibit a broad absorption spectrum, suggesting their potential as an effective semiconductor material for converting light signals into bio-electrical impulses. Supplementary Fig. 1 (see Supplementary Information) shows the photoluminescence (PL) spectra of as-synthesized CTS. The PL spectra show a dominant NIR emission peak, with a shoulder peak about 650–700 nm.

Smart capacitive behaviour of CTS under light illumination

The artificial retina network requires a self-adjusting human-made photovoltaic and capacitive cell with a comparable functionality to natural photoreceptors²⁷. In the literature, there are a few attempts to mimic the human eye using light-active semiconductors^{18,28,29}. In general, conductive or resistive-based device strategies are widely used to sense visuals using an artificial approach. However, capacitive neural networks are a precise mimicry of neuronal functionalities and offer a good simulation at low static power consumption. Therefore, we tested the smart capacitive behavior of our CTS QDs in a three-electrode system (Fig. 2a) using artificial cerebrospinal fluid (aCSF) as an electrolyte. Here, the aCSF solution mimics the composition and properties of natural cerebrospinal fluid (CSF), which surrounds the brain and spinal cord, providing essential support and protection to the central nervous system.

Figure 2b reveals the CV curve of the CTS under dark and light illumination. The capacitive response of the CTS QDs in the dark and illuminated with blue light almost overlapped. However, the response marginally improved under yellow light irradiation and significantly increased under red light illumination, indicating smart supercapacitor behavior with the ability to charge when irradiated with light. Meanwhile, there is a lack of redox peaks in the dark, which may be due to the weak or absence of redox reactions between biological media (aCSF) and CTS. However, under illumination, the CV curve unveiled a pair of redox peaks, which could be ascribed to the redox reactions of aCSF with the CTS electrode and an indication of reversible electron transfer between the oxidative and reducing species^{30,31}. The following equations were used to calculate the capacitance and the relative specific capacitance.

Volumetric capacitance (C_v)

$$C_v = \frac{\int IdV}{2[\text{volume of electrode}][\text{potential window}][\text{scan rate}]} \quad (1)$$

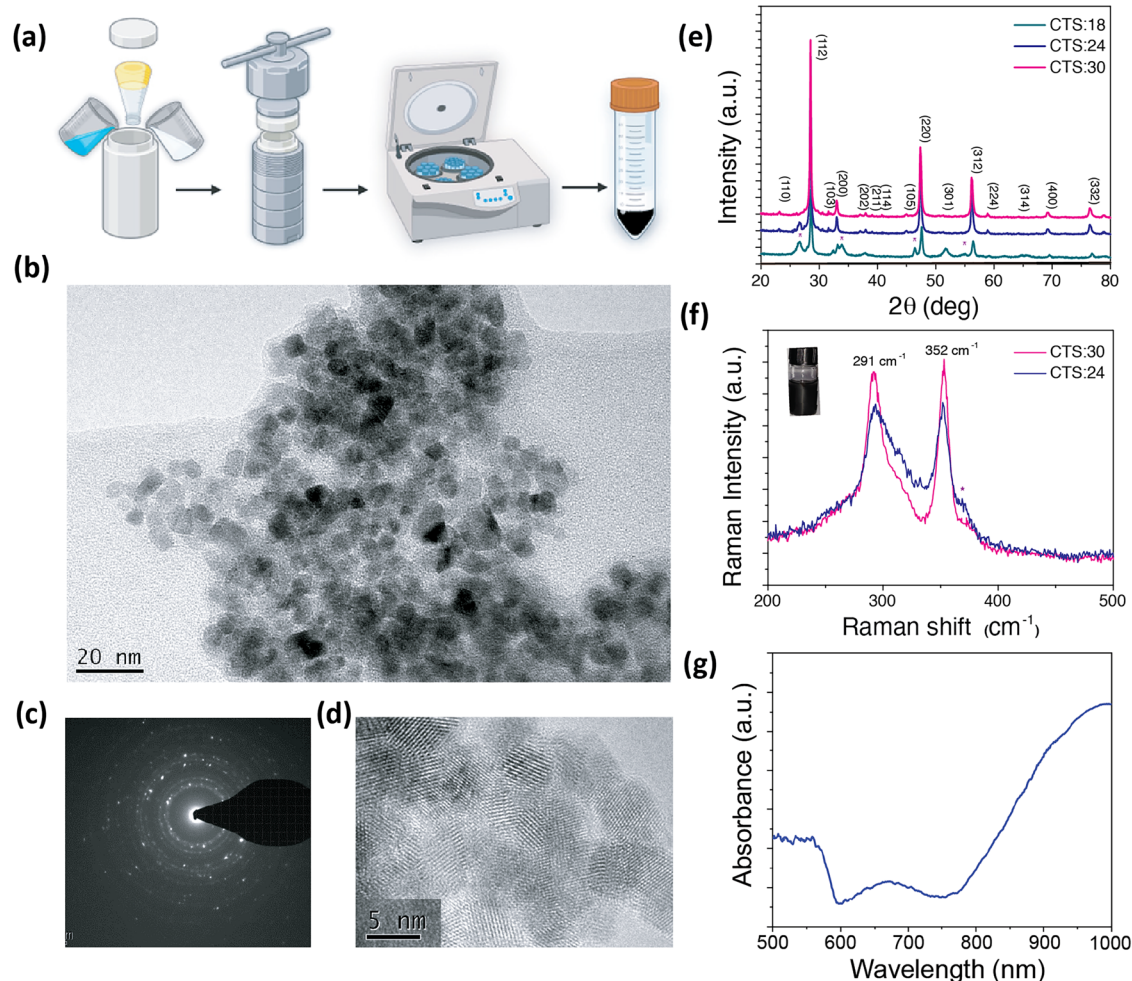


Fig. 1 | Synthesis and characterization of Cu₂SnS₃ (CTS) quantum dots (QDs). **a** A schematic representation of the formation of CTS QDs. The chlorides of copper, tin, and sodium sulphides were used to prepare QDs. The CTS QD inks were prepared in ethanol. The CTS QDs prepared at different deposition time such as 18 (CTS:18), 24 (CTS:24) and 30 (CTS:30) h, **b** TEM image of CTS QDs prepared after 30 h (CTS:30), **c** its selected area electron diffraction (SAED) pattern showing

crystallinity of the product, and **d** HR-TEM showing the ‘d’ spacing of about 0.31 nm, **e** XRD pattern of CTS:18, CTS:24 and CTS:30 samples. As the XRD pattern of CTS:18 and CTS:24 shows impurity peaks (shown by asterisk symbol), while the CTS powder prepared at 30 h shows phase-purity, **f** Raman spectrum of CTS:24 and CTS:30 sample (The inset shows the photographs of CTS-based ink prepared in ethanol), **g** Optical absorbance of CTS:30 sample.

and relative capacitance ($\frac{\Delta C}{C_0}$)

$$\left(\frac{\Delta C}{C_0}\right) \times 100 = \frac{C_{v(light)} - C_{v(dark)}}{C_{v(dark)}} \times 100 \quad (2)$$

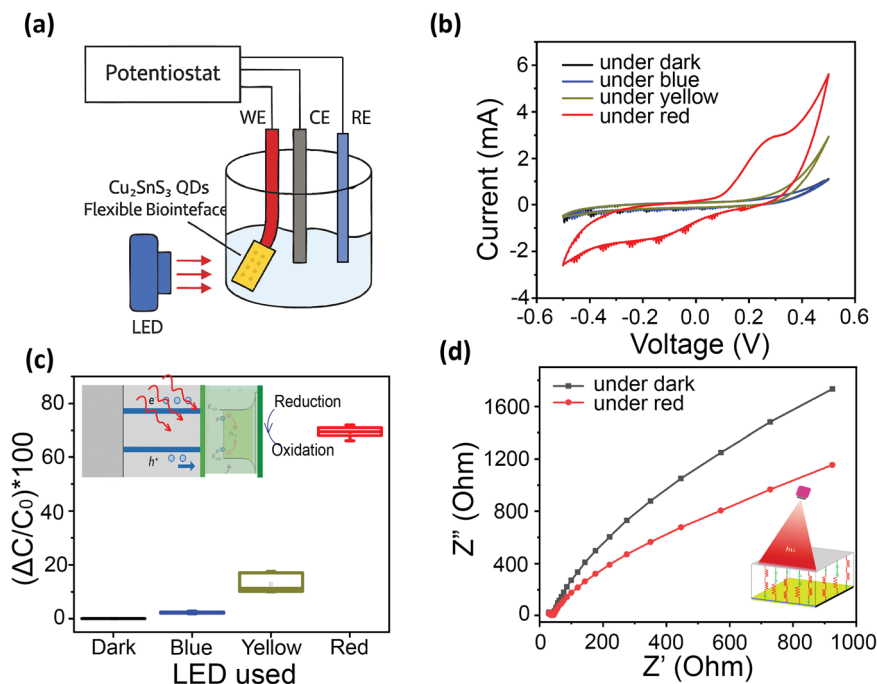
Compared with that in the dark, the relative capacitance of the CTS-based electrode exposed to red light-emitting diodes (LEDs) was approximately sevenfold greater for several independent samples ($n = 3$) (Fig. 2c). We assume that the CTS generates electron-hole pairs through the photoexcitation process and promotes their effective separation under light illumination. As photoexcited charge carriers are mobile, they actively participate in redox reactions at the electrode-electrolyte interface, leading to improved charge storage. Furthermore, due to the higher absorption in this region, the red LED light may interact with more active sites on the CTS electrode, allowing more charge to be stored at the interface, which is critical in neural activation. The mechanism is illustrated in the schematic representation shown in Fig. 2c. The CV reveals the pseudocapacitive nature of the biointerface. Meanwhile, the electrochemical experiment was repeated, and we observed that the relative capacitance of the CTS QDs remained constant even after 1 month, demonstrating their stable performance in aCSF (Supplementary Fig. 2).

In our experiment, similar to CV, we observed the effect of illumination on the impedance of the biointerface (Fig. 2d). In the lower frequency region, the Nyquist plots showed a small, unclear semicircle, whereas at higher frequencies, the semicircle was almost a straight line. Regardless of the LED wavelength, the interface exhibited a similar Nyquist plot. However, the slope of the Nyquist plot increased beyond the knee under light irradiation. This indicates a larger capacitive effect of CTS due to the light exposure. The resistance of the biointerface was decreased under light illumination, with a negligible change in the solution resistance in the high-frequency region. Overall, the electrochemical and impedance measurements together manifest that the response of the CTS was sensitive to the wavelength and intensity of the light, and their behavior confirmed the light-induced increase in capacitance. This system is similar to the natural photoreceptors in the mammalian retina, where the membrane potential varies according to the incident light³².

Configuration and photoelectrochemical supercapacitor performance of the CTS-based biointerface

P3HT and PCBM are commonly employed in organic solar cells, and their combination results in a bulk heterojunction design that allows for efficient charge separation and transport³³. Therefore, we combined CTS with the P3HT:PCBM blend for efficient generation and separation of charges,

Fig. 2 | Photoelectrochemical measurement of Cu_2SnS_3 (CTS) quantum dots (QDs) and their thin film. **a** A schematic representation of the electrochemical measurements set up, **b** Cyclic voltammogram of CTS QDs under the exposure of pulsed blue (450 nm), yellow (530 nm), and red (630 nm) light, **c** Variation of relative capacitance with the light used. The inset shows a schematic representation of photoexcitation, thereby facilitating the effective separation of excitons ($n = 3$). **d** Nyquist plot of CTS QDs-based electrode under dark and red-light illumination. Schematic representation of the conductivity variation of the dielectric medium, an inset figure, as a ladder circuit with a resistor and a capacitor as a function of light.



particularly in the collection of holes, owing to their complementary absorption characteristics and energy level alignment. On the other hand, ZnO facilitates the extraction and transport of electrons generated in the active layer toward the ITO electrode. Therefore, we have harmonized ZnO as an electron and P3HT-PCBM for hole transportation with CTS QDs as the active layer. The biointerface configuration was finalized as 'ITO/ZnO/ Cu_2SnS_3 /P3HT:PCBM' for the photostimulation of retinal neurons (Fig. 3a)^{34–37}. The device features a nanoscale grain size distribution with an ~ 1.3 μm thick absorbing layer (Fig. 3c).

The photoactive nanostructured CTS layer generates electron-hole pairs upon irradiation with visible light, and its integration with ZnO and P3HT supports the dynamic separation of excitons. In the meantime, the p-type conductivity of CTS and the n-type conductivity of ZnO aid in effective charge separation by forming depleted heterojunctions. From the neural prosthesis perspective, such a depleted or excitonic heterojunction leads to the generation of a suitable capacitive response, inducing a displacement current. Moreover, owing to the higher HOMO (highest occupied molecular orbital level) of the P3HT layer at the CTS/P3HT junction, additional separation of the photogenerated charges occurs, and its biocompatible nature is suitable for neural interfaces³⁸.

The smart photocapacitive performance of the CTS-based biointerface was assessed via CV and transient photocurrent measurement using a three-electrode configuration. The comparative CV curves under dark and red-light illumination are shown in Supplementary Fig. 3, with the area contained in the CV curve indicating greater charge storage under light illumination. This increased charge is ultimately available for injection by short pulses at the neural interface³⁹ and to reduce electrode noise due to resistive charge transfer elements⁴⁰. When we compared the CV of pristine CTS and the biointerface (Fig. 2b and Supplementary Fig. 3), interestingly, we observed some noticeable discrepancies, including an increased number of oxidation peaks and slight shifts in the CV curve of the biointerface. Within the CV curves of the biointerface, two distinct oxidation peaks prominently emerged. These results are due to the surface modification of the CTS electrode, which is sandwiched between the ZnO and P3HT:PCBM layers and subsequently undergoes multielectron oxidation processes. When ZnO, CTS, and P3HT:PCBM are stacked together, their electronic properties can influence each other, and thereby, the energy levels of the materials shift due to charge transfer

and electronic coupling at the interfaces. In connection with this, we believe that the interfaces may introduce new energy states that can affect the redox processes in CTS, leading to a slight shift in the oxidative peak potential. Light may affect the generation of photoinduced redox reactions⁴¹. This may suppress charge recombination by facilitating the separation of charge carriers and prolonging their lifetimes, thereby increasing the probability of effective charge transfer during cycling. Meanwhile, with light irradiation, the orientation of the CV curves of both the pristine CTS and the biointerface becomes slightly vertical. In a previous work, we reported such a shift in orientation owing to light irradiation⁴². Further, we investigated the cyclic stability of the CTS electrode in oxygenated aCSF at 37 °C, for 500 cycles and found good capacitive retention (Supplementary Fig. 4).

To understand the charge-carrier dynamics of the CTS-based biointerface, we measured the transient photocurrent under red light (625 nm) from a short-pulse excitation (Supplementary Fig. 5). The photocurrent exhibits characteristics of light-on and light-off spikes, accompanied by significant charge generation. The rise and fall times are insignificant compared with the charge hold time of about 200 ms. These fast charging and discharging dynamics indicate superior charge transfer at the CTS biointerface-aCSF electrolyte boundary and the onset rate of the reaction, confirming the capacitive nature of the device^{43,44}. Meanwhile, to further understand the roles of each bio-interface component, we investigated photocurrent in ZnO, ZnO/CTS, ZnO/P3HT:PCBM, and ZnO/CTS/P3HT:PCBM (Supplementary Fig. 6a). Although the P3HT:PCBM generates slightly higher photocurrent in aCSF than CTS, but it lagged much behind in capacitive tests (Supplementary Fig. 6b, c). However, P3HT:PCBM and CTS harmonize to convert light energy into electrical energy while also storing charge.

The induced charge is a critical parameter for stimulating human tissues such as the subretinal-thalamic nucleus and the cortical region of the brain⁴⁵. Supplementary Fig. 5 shows a photogenerated charge density of around $9 \mu\text{C}/\text{cm}^2$ under red light at $8 \text{ mW}/\text{cm}^2$. This value is two to three orders of magnitude greater than the minimum required charge density. Meanwhile, the observed value is significantly lower than the tissue damage thresholds for material-based devices^{46,47}. Additionally, the theoretical aspects and computations required for the minimal charge density are described in the supplementary information. The energy efficiency and

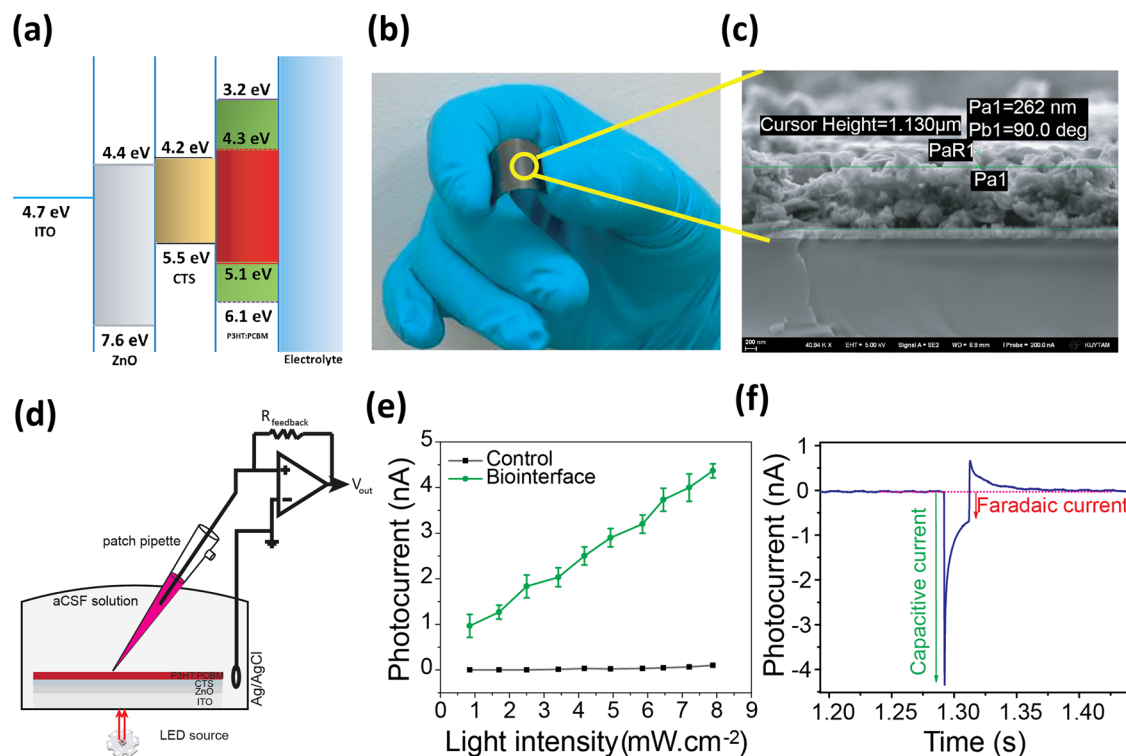


Fig. 3 | Characterization of biointerface in free-standing mode. **a** The electronic energy levels of components of CTS based biointerface with respect to vacuum level, **b** photograph of a flexible CTS based biointerface deposited on ITO-coated PET substrate, **c** cross-sectional SEM images of biointerface showing the thickness of different layers, **d** The schematic representation of photocurrent measurement at

free-standing mode, **e** photocurrent generated by CTS QDs based biointerface under different illumination intensities of 20 ms of red light, **f** photocurrent transient response under red LED illumination showing contribution of capacitive and Faradaic current under illumination 20 ms of red light at 8 mW/cm².

energy per pulse are crucial for neural interfaces; thus, we calculated them and presented them in the supporting information.

In the context of retinal stimulation, the foremost criterion of the biointerface is not limited to generating controlled and localized electrical currents; it can also operate independently to respond to incident light without relying on external power sources or wired connections. This autonomy is crucial for practical implementation. Therefore, we have tested the photoelectrical performance of a CTS-based biointerface in free-standing mode (without wire connections) using a patch-clamp electrophysiology system. To mimic the retinal atmosphere, we have floated the CTS-based biointerface device in aCSF, and a micro patch pipette was situated over the device without physical contact. This micro-patch pipette contains an intracellular medium. Figure 3d shows a schematic representation of the experimental setup used to measure the photoactivated electrical signal in a biological medium.

The CTS-based biointerface device accomplished a maximum photocurrent of 4.5 nA when illuminated with red LEDs at a low intensity of 8 mW/cm² (Fig. 3e). Figure 3f shows the free-standing photocurrent profile under the tested LED source at 8 mW/cm². In particular, when the LED is turned on rapidly, the interface undergoes a change in the local electric field, as well as charge separation and distribution. This will result in displacement or capacitive current with a short time constant, as seen in Fig. 3f. When the LED is switched off, the charge generation, separation, and distribution processes are disrupted, causing charges to recombine. Meanwhile, a faradaic current is generated when charges interact with redox-active species, electrolyte, or reactive surface states, causing a positive peak^{48,49}. In our case, photocurrent comprises a majority of capacitive transient shapes, with ~15% contributing to the Faradaic current. It is well known that the capacitive current is vital in neural stimulation owing to perturbation by electromagnetic charge-ion interactions³⁵. The ITO without a biointerface (control) and current under multiple illuminations of the biointerface

presented in Supplementary Fig. 7 validate this behavior. Meanwhile, similar to the results of the photoelectrochemical measurement (Supplementary Fig. 5), the fast charging dynamics were also observed in the electrophysiological setup, with the current time increasing in the order of microseconds and the decay time in the range of milliseconds, in contrast to the longer rise and fall times for the faradaic component⁵⁰. Further, we extracted carrier lifetime from the transient photocurrent (Supplementary Fig. 7b) by fitting the post-peak decay to a single-exponential model as presented in the supplementary information section. After converting the photocurrent to its magnitude and using nonlinear least squares, the decay constant was found to be about 100 μs. This value indicates the fast photocarrier extraction, which is beneficial for quick neuronal activation. Meanwhile, we tested the response of the CTS biointerface-based device for blue (450 nm) and green/yellow (530 nm) LEDs as well (Supplementary Fig. 8). In contrast to the response to red LEDs, light with a 530 nm wavelength produces a moderate response and light of 450 nm produces very low photocurrent. Our measurements provide complete spectral characterization and confirm that red light is the optimal wavelength range for wireless capacitive stimulation in this CTS-based system. Therefore, subsequent experiments were performed at 530 nm (green/yellow) and 630 nm (red) to capture the device response across the most effective part of its operating spectrum.

Moreover, the following equation is used to calculate the loss or gain of heat (*q*) by a CTS-based biointerface to study the influence of photothermal excitation^{35,51}.

$$q = m \cdot c \cdot \Delta T \tag{3}$$

where *c* is the specific heat, *m* is the mass of the sample, and ΔT is the temperature change. The calculated change in the temperature (°C) is much less than that required (>5 °C) for photothermal excitation. This value

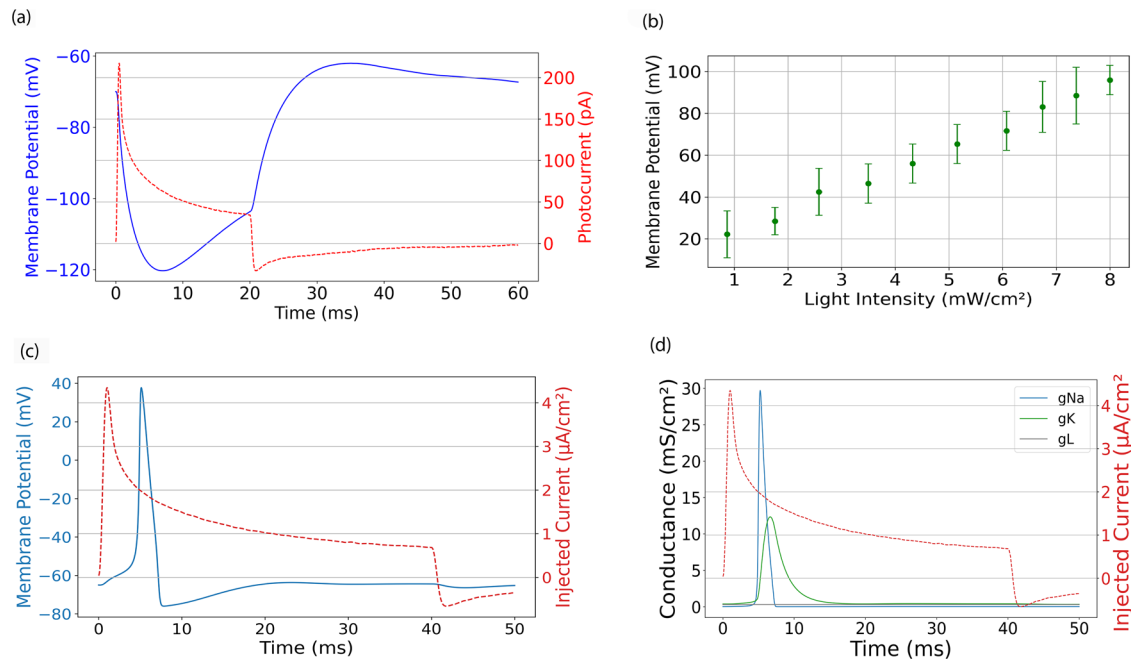


Fig. 4 | Simulation of the transmembrane potential in passive mode. **a, b** Simulated membrane potential dynamics of a passive cell membrane upon photocurrent stimulation, corresponding to the measured photocurrent with the patch-clamp set-up shown in (b, c). The model incorporates a passive RC circuit representing the cell membrane, with stimulation applied through the basal contact area on a freestanding electrode. The resulting depolarization reflects the capacitive

charging of the membrane in response to transient photocurrent pulses. **c** Transmembrane potential (V_m) response of the Hodgkin–Huxley model to a time-dependent inward photocurrent stimulus. **d** Time-resolved ionic conductances (g_{Na} , g_K , and g_L) and the inward photocurrent input used to stimulate the Hodgkin–Huxley model (membrane capacitance (C_m)=1.0 $\mu\text{F}/\text{cm}^2$, g_{Na} = 120 mS/cm^2 , g_K = 36 mS/cm^2 , the leak conductance was g_L = 0.3 mS/cm^2).

confirms the lack of influence of photothermal excitation on bioelectrical signal generation at our CTS-based biointerface.

Simulation of the transmembrane potential

In the passive cell model simulation, we model the transmembrane potential (V_m) dynamics of an SH-SY5Y cell cultured on a freestanding electrode using a passive RC circuit approach⁵². The cell is treated as a spherical capacitor with a membrane capacitance of 6.8 pF and resistance of 0.8 G Ω , yielding a membrane time constant ($\tau \approx 5.4$ ms) that governs the voltage response to photoelectrical stimulation through a free-standing photocapacitor. The total membrane surface area is estimated based on the spherical geometry of the cell, while the junctional membrane area (A_{jm}), representing the portion of the membrane in contact with the electrode, is approximated as 20% of the total surface area, consistent with the footprint of a normally spread adherent cell. The photocurrent is applied exclusively through this contact area. For the final simulation shown in Fig. 4a, we used a temporal resolution of 10 μs to ensure accurate modeling of the sub-millisecond RC charging behavior. The transmembrane voltage was computed using the exponential charging relationship: $\Delta V_m(t) = -R_m I_{\text{photocurrent}} (1 - e^{-t/\tau})$, which captures the capacitive charging of the membrane, and the resulting transient depolarization observed during each photocurrent pulse. This passive model provides a biophysically grounded description of membrane polarization dynamics and predicts voltage excursions up to several tens of millivolts (approaching 95 mV) under strong photoelectrical or electroporative stimulation conditions (Fig. 4a, b). Physiological depolarization is normally limited to ~30–40 mV, whereas biophysical stimulation through transient capacitive charging can induce brief voltage excursions up to ~80–100 mV without causing irreversible membrane damage.

Furthermore, the Hodgkin–Huxley (H-H) model is a biophysically detailed mathematical framework that describes how action potentials in neurons are initiated and propagated through the dynamic behavior of voltage-gated ion channels. The time-dependent external stimulus current (I_{inj}) was derived directly from a photocurrent time-response curve

provided in an Excel file, where the input was reversed (to model inward current). This stimulus was used to simulate the evolution of the membrane potential and ionic conductance over time in response to physiologically realistic light-induced photocapacitive currents. The following equation is the dynamic membrane potential response of a real neuron to an injected photocapacitive current^{53,54}:

$$C_m \frac{dV}{dt} = I_{inj}(t) - I_{Na} - I_K - I_L \tag{4}$$

This equation describes how the membrane capacitance C_m integrates the net current, where the change in membrane potential over time is driven by the injected current $I_{inj}(t)$ and opposed by the ionic currents from sodium (I_{Na}), potassium (I_K), and leak channels (I_L). In our simulation, we consider a photocurrent density of 4 $\mu\text{A}/\text{cm}^2$ generated by the photocapacitor or solar cell interface as $I_{inj}(t)$. If only 5% of the total generated current is effectively coupled into the cell membrane, this corresponds to an injected current density of 200 nA. Despite this fractional coupling, the resulting transmembrane current is still well above the threshold required to trigger action potentials in a Hodgkin–Huxley neuron model, where spike initiation typically occurs for injected currents on the order of 10–20 nA. This indicates that even partial current transfer from a photoactive interface is highly sufficient to induce robust neuronal firing, confirming the efficacy of such stimulation approaches in driving bioelectrical excitability. The temporal evolution of the membrane potential and the corresponding ion channel conductance in response to the photocurrent stimulus are illustrated in Fig. 4c, d.

Calcium imaging of neurons to study the efficacy of neural stimulation

Calcium imaging is a vital tool for studying the effects of light stimulation on the bioelectrical properties of neurons and for visualizing and tracking neural activity in living cells in real-time. To ensure the safe stimulation of retinal neurons, we first performed a toxicity experiment. Primary

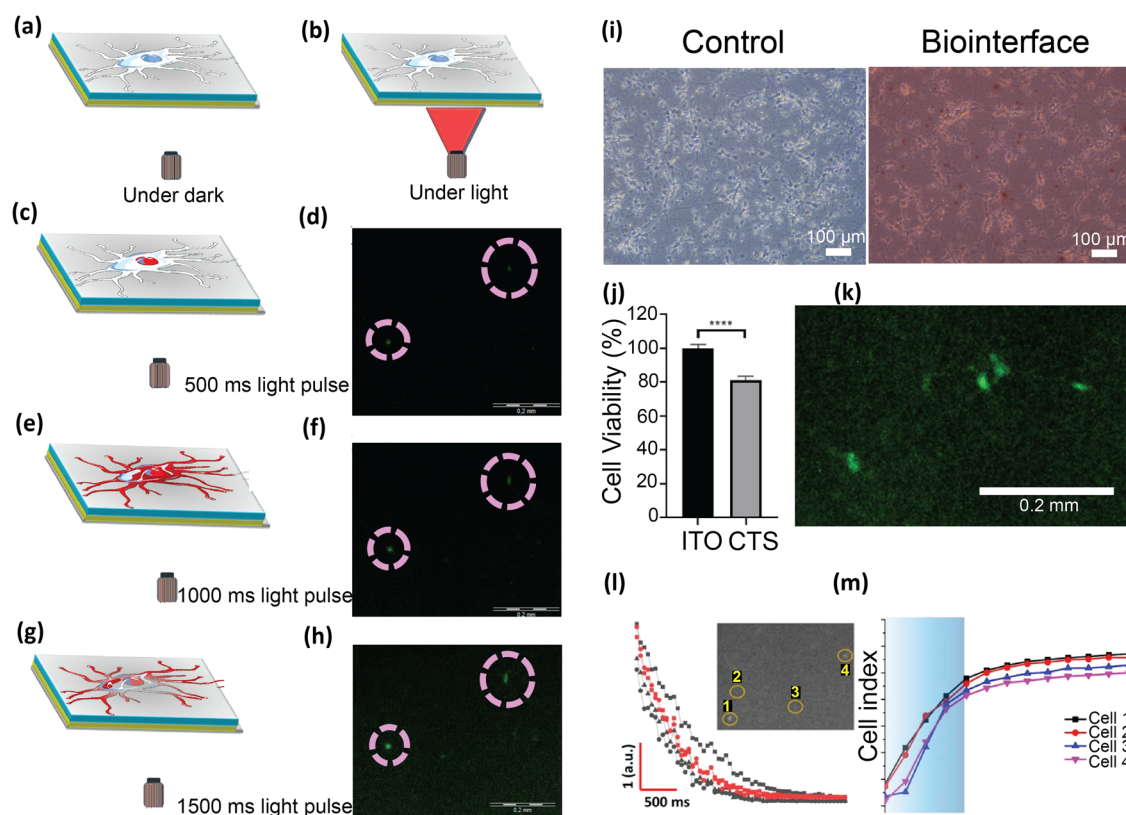


Fig. 5 | Time-lapse calcium imaging for the efficacy measurement of the photo-electrical stimulation. The schematic representation shows the steps during the neurons excited by the red-light illumination and respective calcium imaging showing the activity of individual neurons including **a** the cells over CTS based biointerface before light excitation, **b** the incidence of red light on the biointerface, **c** excitation of cells after 500 ms light-off, **d** the images were taken after a light pulse was turned off (after 500 ms), **e** the schematic showing the progression of the photo-bioelectrical signal generation in the neuron after 1000 ms (light-off), **f** corresponding calcium image after 1000 ms showing neuron activity, **g, h** schematic and calcium image of neurons after 1500 ms of light-off. The selected region (circle) in **d, f, h** shows the activities of neural cells, **i** The fluorescence images

of primary hippocampal neurons on control (ITO) and CTS-based biointerface, **j** MTT biocompatibility assay analysis data are presented in a column graph plotting the mean with the standard deviation ($N = 4$ and Control), **k** The calcium image reveals optically modified neural network dynamics. The fluorescent images of hippocampal neuron loaded with Fluo-4 AM cultured on CTS based biointerface and optically excited at 625 nm, **l** the calcium signal trace of four representative neurons after 2000 ms of light-off, the inset shows the images of hippocampal neurons and the selected region (circle) shows the location of the neurons, and **m** calcium imaging traces of neurons after turning on the light. The time for the highlighted region is about 1 s.

hippocampal neurons were used in a 3-(4,5-Dimethylthiazol-2-yl)-2,5-diphenyltetrazolium bromide (MTT) cell viability assay to assess the biocompatibility of the CTS-based biointerface, with bare ITO samples serving as the control. The CTS-based biointerface device exhibits a cell survival rate of about 80% (Fig. 5i, j). It is well known that cell viability below 30% implies significant cytotoxicity, whereas about 80% or above shows negligible or minimal cytotoxicity⁵⁵. Supplementary Fig. 7 also confirms the photograph of healthy hippocampal neurons grown over the CTS-based biointerface.

In our study, an excitation pulse of 20 ms of yellow light (530 nm) at 10 mW/cm² and red light (630 nm) at an intensity of 8 mW/cm² were applied separately to hippocampal neurons to study their cellular calcium dynamics in vitro. The CTS-based biointerface excites the cells, causing an influx of calcium ions. The fluorescent indicators then bind to these calcium ions, emitting light and producing a measurable fluorescence signal (Fig. 5a–h, k). After the light pulse was switched off, images were captured. During the initial stage, the fluorescence signal is low; therefore, the neurons are not clearly visible under the microscope owing to an increase in calcium levels (Fig. 5i and Supplementary Fig. 9). The response of the neurons is still in the process of attaining a steady state during the second phase (after 1000 ms of light stimulation), and the signal may not have stabilized entirely. As a result of the weaker and fluctuating fluorescence signal during this phase, the neurons may seem indistinct under the microscope (Fig. 5e, f). However, the calcium concentration has achieved a plateau in the third stage, resulting in a steady and higher fluorescence signal, and the neurons

on the microscope screen become more apparent and identifiable (Fig. 5g, h). These images display the variations in fluorescence intensity resulting from neuronal activity, which leads to an increase in intracellular calcium levels.

The hippocampal neurons were also activated by yellow light, and Supplementary Fig. S9 shows the corresponding time-lapse calcium imaging, revealing optically modified neural network dynamics. Figure 5k shows a calcium image of the CTS-based biointerface activated by red light illumination. The green patches in the image indicate activated neurons with elevated calcium levels. The bioelectrical signal generated by the CTS-based biointerface stimulates the firing of neurons, which become electrically active and transmit action potentials. However, neurons require time to activate and calcium ions to enter them. Figure 5m depicts the calcium imaging traces of neurons shortly after turning on the light. Similarly, time is necessary for the neurons to reach the baseline intake of calcium ions, which is after 2000 ms of light-off (Fig. 5l). Meanwhile, the hippocampal neurons were also activated by green/yellow light (530 nm) as well as red light (630 nm) of intensity of 1 mW/cm² and Supplementary Figs. 9 and 10 show the corresponding time-lapse calcium imaging, revealing optically modified neural network dynamics.

To quantify the results of the analysis, we plotted the relative fluorescence over time, thereby calculating the $\Delta F/F_0$ ratio by recording the fluorescence intensity of the images of hippocampal neurons loaded with Fluo-4 AM. The relative fluorescence over time for different regions of

interest (ROIs) within cells was measured and is presented in Supplementary Fig. 11a. The increase in fluorescence is calculated as the difference between the mean of the peak and the mean of the measurements of frames after subtraction of the background signal. This graph provides insight into how fluorescence changes over time within different cellular areas, which can be valuable for studies in cell biology and for observing dynamics in real time. In our case, fluorescence increases over time and reaches its maximum value when the cells are visible under the microscope. Furthermore, the resting or baseline calcium levels in neurons, known as F_0 (the initial fluorescence intensity), are measured without light stimulation. The fluorescence intensity of the optically activated neurons was subsequently recorded, and the corresponding change in fluorescence intensity (ΔF) is shown in Supplementary Fig. 11b. In our case, the $\Delta F/F_0$ value is $\sim 10\%$, which indicates an increase in fluorescence intensity relative to the baseline, indicating concentration variations in intracellular calcium, which enables the study of the temporal dynamics of calcium ions over time. Overall, the increased calcium influx proves the effective photostimulation of hippocampal neuron cells by the CTS QDs-based biointerface device. Thus, we have demonstrated that the Cu_2SnS_3 -based photocapacitor biointerface combines solar cell and supercapacitor technologies for retinal stimulation. This allows for efficient energy storage, quick charge/discharge, and increased neuron activation under visible light. However, for long-term stability, the device architecture must be optimized by improving the charge transport layers and fine-tuning the band alignment. The human retina is extremely sensitive and can detect illumination of the order of few tens of photons per photoreceptor per second under scotopic (low-light) conditions. Furthermore, the red LED's light intensity to excite neurons is about 8 mW/cm^2 , which provides roughly 10^{15} – 10^{16} times the number of photons per pulse needed for the bare minimum of visual perception. This is to be expected given the huge phototransduction advantages through molecular amplification achieved by biological photoreceptors via enzyme cascade and brain integration. However, this gap could be reduced by using an optical concentrator, designing device topologies with internal photomultiplication, forming tandem cells, and employing ligand exchange for effective charge separation and extraction.

Discussion

We used Cu_2SnS_3 -based photocapacitor biointerface devices to combine solar cell and supercapacitor technologies for hippocampal neuron stimulation systems. The device stores electrical energy by accumulating charge on the electrodes in accordance with the incident light's wavelength. When illuminated by visible light, the biointerface device displayed a good free-standing photoresponse with a capacitive current. The supercapacitor behavior of the device allows for quick charge and discharge as well as instantaneous energy availability, whereas solar cells allow for energy harvesting. This integrated technique improves the overall efficiency of the stimulation device, as indicated by calcium imaging of hippocampal neurons. This study suggests that CTS-based light-induced biointerfaces are a viable material for wireless retinal implants. Moreover, the flexible quantum dot-based photocapacitive biointerface introduced in this study holds strong potential for integration into next-generation wearable neuromodulation systems and photoactivated ion pumps. The device's soft, conformable architecture, enabled by the organic-inorganic hybrid of Cu_2SnS_3 QDs and P3HT:PCBM, supports seamless interfacing with biological tissue, making it ideal for epidermal electronics or subretinal implantation. Its operation under low-intensity red light and stable electrochemical response across multiple stimulation cycles further underscores its long-term durability and safety in dynamic physiological environments. These attributes position the device as a scalable platform for wireless bioelectronic therapeutics, enabling spatiotemporally precise ionic or neural control without the need for external wiring or batteries. Furthermore, similar light-activated semiconductor devices are being increasingly investigated for cancer therapy, particularly for targeted tumor modulation and phototherapy^{56,57}.

Methods

Preparation of CTS QDs

The chemicals, including copper chloride (CuCl_2), tin chloride (SnCl_2), sodium sulphide (Na_2S), and ethylenediamine, were purchased from SD Fine Pvt. Ltd, India, and used as received. Monodisperse CTS nanoparticles were successfully synthesized by the simplistic solvothermal technique at 210°C for various reaction times (18, 24, and 30 h). In a precursor solution, 20 mM CuCl_2 , 10 mM SnCl_2 , and 30 mM Na_2S were added to 33 mL of deionized water and 7 mL of ethylenediamine under vigorous stirring for 2 h to improve the homogeneity. The product was washed with excess isopropyl alcohol in toluene several times to purify the CTS product. The CTS ink was prepared by dissolving about 100 mg of CTS QD powder in a 1 mL ethanol solution.

High-resolution powder X-ray diffraction with Ni-filtered Cu-K α 1 (Bruker D8 Advance X-ray diffractometer) was used to study the structural properties of the CTS QDs. The micro-Raman spectra of the CTS samples were recorded in the range of 150 – 600 cm^{-1} using a micro-Raman spectrometer (LabRam HR800 UV Raman microscope, Horiba Jobin-Yvon, France at KBSI, Gwangju Centre) with a He-Ne laser source with an excitation wavelength of 514 nm and a resolution of 0.3 cm^{-1} at 10 mW laser power. The surface morphology of the produced product was recorded using a field emission scanning electron microscope (FE-SEM; S-4700, Hitachi). The TEM images were examined using a JEOL-3010 instrument with a 300 kV operating voltage. High-resolution TEM (HRTEM) pictures were captured using a Tecnai G2 F20 with a 200 kV operating voltage. XPS (VG Multilab 2000, Thermo VG Scientific, UK) with a monochromatic Mg-K α (1253.6 eV) radiation source was used to determine the chemical bonding. The carbon 1s line, which corresponds to 285 eV, was utilized to calibrate the binding energies in the spectrometer. At room temperature, optical absorption of the powder samples was performed via an ultraviolet-visible-near-infrared (UV-Vis-NIR) spectrophotometer (Cary 100, Varian, Mulgrave, Australia). The photoluminescence (PL) spectra were recorded using a closed-cycle liquid helium cry generator (APD, SH-4, USA) and a spectrometer ($f = 0.5 \text{ m}$, Acton Research Co., Spectrograph 500, USA).

Fabrication of CTS-based supercapacitor biointerface

An ultrasonicator was used to purify the ITO-coated glass substrates that were purchased from Ossila, using deionized water, detergent, acetone, isopropanol, and a 15-min UV ozone treatment. The zinc oxide (ZnO) hole-blocking layer was applied over the ITO substrate using a spin-coater at 2000 rpm for 60 s using precursors such as 219 mg of zinc acetate and 90 mg of ethanolamine in 2 ml of 2-methoxyethanol. After spin coating with ZnO, the substrate was annealed for 15 min at 300°C , and then the CTS QDs were spin-coated on top of the ITO/ZnO at 1500 rpm for 30 s. Further, the ITO/ZnO/CTS film was baked for half an hour at 300°C . Furthermore, the P3HT:PCBM solution prepared in *o*-dichlorobenzene was deposited over ITO/ZnO/CTS using spin coating at 1500 rpm for 180 s. Finally, the device was placed over a hot plate maintained at 150°C for 15 min to eliminate the solvent.

Photoelectrochemical analysis of the CTS QDs and biointerface

An Autolab Potentiostat Galvanostat (PGSTAT302N, Metrohm, Netherlands) was used for the electrochemical measurements of the CTS-based biointerface, and NOVA software was used to calculate the electrical parameters. For the capacitance-voltage measurements under various light illuminations, a three-electrode configuration was used, consisting of a platinum rod as the counter electrode, an Ag/AgCl reference electrode, and a CTS-based interface as the working electrode with aCSF used as an electrolyte. The aCSF mimics the fluid present in the human brain and is prepared with 10 mM 4-(2-hydroxyethyl)-1-piperazineethanesulfonic acid (HEPES) and glucose, 2 mM CaCl_2 , 140 mM NaCl, 1 mM MgCl_2 , and 3 mM KCl in distilled water. By injecting a stoichiometric quantity of NaOH, the pH of the aCSF solution was kept at around 7.4. Further, the electrochemical impedance spectroscopy potential scan mode was utilized to test the impedance of the CTS-based bio-interface under different light

sources. In the experiment, the LEDs (Thorlabs, NJ, USA) were used as a light source with different wavelengths, such as blue LED with a wavelength of 445 nm (M450LP1), green LED with a wavelength of 530 nm (M530L3), and red LED with a wavelength of 630 nm (M630L3). The full-width half-maxima of blue, green, and red-light spectrums are 16.7 nm, 33.3 nm, and 13.4 nm, respectively, and are consistent with a previous report. The LEDs were driven by a DC2200 High-Power 1-Channel LED Driver with Pulse Modulation (Thorlabs, NJ, USA). To measure the approaching power of light at the CTS-based biointerface, a power meter (Newport 843-R) was used. Meanwhile, for all the electrochemical tests, a 1 cm² area of the CTS-based biointerface device was submerged in aCSF.

To investigate the ability of a biointerface to induce a purely light-activated current and charge without the use of wires, we floated the CTS device in aCSF and measured the current and voltage as a function of the wavelength and power of the light using an EPC 800 Heka Elektronik patch-clamp amplifier. To imitate the real neural network in human eyes, a pipette filled with an intracellular medium was put over the biointerface without touching. In distilled water, 140 mM KCl, 2 mM MgCl₂ and Mg-ATP, 10 mM HEPES, and ethylene glycol-bis (-aminoethyl ether)-N,N',N'-tetraacetic acid (EGTA) were mixed to make the intracellular medium. A KOH solution was used to maintain the pH of the intracellular solution between 7.2 and 7.3.

Primary neuron isolation and electrophysiology recordings

The procedure used for primary neuron isolation has been approved by Koc University's Institutional Animal Care and Use Committees (Approval No: 2019.HADYEK.023) in accordance with the resolution issued by the European Parliament and Council Directive 2010/63/EU on the Protection of Animals Used for Scientific Purposes. The retinal origin neurons, namely the Hippocampal cells, were isolated from decapitated E15-E17 Wistar Albino rats and placed in ice-cold Hank's Balanced Salt Solution (HBSS, Thermo Fisher Scientific, MA, USA). The hippocampi were incubated at 37 °C in 0.25% Trypsin-EDTA solution (Thermo Fisher Scientific, MA, USA) with 2% DNase-I supplement (NeoFroxx, Einhausen, Germany) for 20 min. The cells were then centrifuged, and the supernatant was replaced with Dulbecco's Modified Eagle Medium/Nutrient Mixture F-12 (DMEM/F12 Thermo Fisher Scientific, MA, USA) supplemented with 10% foetal bovine serum (FBS, Heat Inactivated, GE Healthcare, IL, USA) and 1% penicillin/streptomycin (Thermo Fisher Scientific, MA, USA). DMEM/F12 was removed, and Neurobasal Medium (NBM, Thermo Fisher Scientific, MA, United States) supplemented with B27, L-glutamine, β-mercaptoethanol, and glutamate (Thermo Fisher Scientific, MA, United States) was added to the cell pellet. The cells were triturated before being strained through a 70 μm cell strainer. The homogeneous cell solution was seeded on poly-D-lysine (PDL) coated substrates (Sigma-Aldrich, MO, USA). After three days of incubation in a 37 °C incubator with 5% CO₂, the media of the cells on substrates were changed to NBM enriched with cytosine arabinoside (Sigma-Aldrich, MO, United States) to limit glial cell proliferation. After a 24-h incubation with cytosine arabinoside, the medium was replaced with NBM, and the hippocampal neurons' substrates were employed for tests. The Olympus T2 upright microscope's built-in digital camera was used to monitor the patch pipette and cells.

Biocompatibility assay

Hippocampal primary neurons' biointerface cell viability was examined using the MTT viability test (ab211091, Abcam, Cambridge, UK). Using Neurobasal medium with B27 supplementation, the neural growth medium was created. Before sterilization, the devices were cleaned with 70% ethanol, then dried by air. The surface was then further sterilized for 30 min using UV light. The six-well plates' wells were filled with substrates, and neurons were seeded on the substrates in B27-supplemented Neurobasal media. Following the removal of the B27-supplemented Neurobasal medium, the neurons were cultured in the neuron growth medium for 48 h. After that, the media were changed and each well received 4 ml of NBM mixture and

1 ml of MTT solution (5 mg/ml in PBS, pH = 7.3). The cells were then incubated at 37 °C and 5% CO₂ for an additional 4 h. Then the substrates were transferred to empty six-well plates after the medium in each well was sucked out. To dissolve the formazan crystals, a 1:1 combination of DMSO and ethanol was poured into each well. The solution was transferred to a 96-well plate, and the absorbance was measured at 570 nm using a Bio-Tek Instruments Synergy H1 Micro-plate Reader. Viability = (OD_{sample}/OD_{control})*100 was used to calculate relative cell viability. The optical density (OD) of the sample was measured using cells grown on a photo-electrode, while the OD of the control was measured using cells grown on ITO substrates.

Calcium imaging

Following the technique detailed in the Primary Neuron Isolation section, primary hippocampus cells were seeded onto sterilized photoelectrodes and non-coated conducting glass substrates. Following that, the cells were cultured for 24 h in full growth media at 37 °C and 5% CO₂. Acetoxy-methyl-ester Fluo-4 (Fluo-4AM) was used in conjunction with pluronic acid F-127 for calcium imaging. A final working concentration of 1 μM Fluo-4AM was added to the medium, and the cells were incubated in the dark for 30 min at 37 °C and 5% CO₂, followed by 15 min at room temperature. Following that, the Fluo-4AM-containing medium was replaced with new full medium. Following a 30-min rest period, the cells were stimulated with 24 mW light pulses with a period of 2 s and a duty cycle of 50%. For imaging, an OlympusPro IX71 outfitted with an AndoriXon EMCCD camera was used, with excitation and emission wavelengths of 450, 530, and 630 nm, respectively. The obtained pictures and movies were analyzed using the Fiji ImageJ (NIH) program. The ROI Manager program was used to randomly choose 10 cells, and the Multi Measure option was utilized to take time-lapse fluorescence intensity data. Fluorescence intensities (grey values) were measured, and background noise was removed from the computed means to get the dF/F value. F is the beginning fluorescence intensity at time zero. dF/F was used to calculate the final fluorescence ratio change. $dF/F = 1$ signified a resting intracellular calcium concentration, whereas upward deflections indicated an increase in intracellular calcium concentration and consequent depolarization.

Data availability

The datasets generated and/or analyzed during the current study are not publicly available due to proprietary institutional restrictions but are available from the corresponding author on reasonable request.

Code availability

The Python codes for the simulation of the passive RC model presented in the manuscript has been included in the supplementary information.

Received: 31 July 2025; Accepted: 8 January 2026;

Published online: 21 January 2026

References

- Mitchell, P., Liew, G., Gopinath, B. & Wong, T. Y. Age-related macular degeneration. *Lancet* **392**, 1147–1159 (2018).
- Chang, B. et al. Retinal degeneration mutants in the mouse. *Vis. Res.* **42**, 517–525 (2002).
- Cehajic-Kapetanovic, J., Singh, M. S., Zrenner, E. & MacLaren, R. E. Bioengineering strategies for restoring vision. *Nat. Biomed. Eng.* **7**, 387–404 (2023).
- Menon, A. & Vijayavenkataraman, S. Novel vision restoration techniques: 3D bioprinting, gene and stem cell therapy, optogenetics, and the bionic eye. *Artif. Organs* **46**, 1463–1474 (2022).
- Van Gelder, R. N. et al. Regenerative and restorative medicine for eye disease. *Nat. Med.* **28**, 1149–1156 (2022).
- Karatam, O. et al. Optical neuromodulation at all scales: from nanomaterials to wireless optoelectronics and integrated systems. *Chem. Soc. Rev.* **52**, 3326–3352 (2023).

7. Mohammadiaria, M. & Srivastava, S. B. Metasurface-assisted bioelectronics: bridging photonic innovation with biomedical implants. *Light Sci. Appl.* **14**, 386 (2025).
8. Mohammadiaria, M., Rathbun, D. L., Kamita, M. & Srivastava, S. B. Mechanistic insights into excitonic and electrostatic stimulation of cells by photovoltaic substrates/nanocrystals and through light polarization modulation. *PLoS ONE* **20**, e0335978 (2025).
9. Gilja, V. et al. Challenges and opportunities for next-generation intracortically based neural prostheses. *IEEE Trans. Biomed. Eng.* **58**, 1891–1899 (2011).
10. Regan, D. Visual processing of four kinds of relative motion. *Vis. Res.* **26**, 127–145 (1986).
11. Jiang, Y. & Tian, B. Inorganic semiconductor biointerfaces. *Nat. Rev. Mater.* **3**, 473–490 (2018).
12. Airaghi Leccardi, M. J. I. et al. Photovoltaic organic interface for neuronal stimulation in the near-infrared. *Commun. Mater.* **1**, 21 (2020).
13. Miyasaka, T. & Murakami, T. N. The photocapacitor: An efficient self-charging capacitor for direct storage of solar energy. *Appl. Phys. Lett.* **85**, 3932–3934 (2004).
14. Jin, W. Y., Ovhal, M. M., Lee, H. B., Tyagi, B. & Kang, J. W. Scalable, all-printed photocapacitor fibers and modules based on metal-embedded flexible transparent conductive electrodes for self-charging wearable applications. *Adv. Energy Mater.* **11**, 2003509 (2021).
15. Vijjapu, M. T. et al. A flexible capacitive photoreceptor for the biomimetic retina. *Light Sci. Appl.* **11**, 3 (2022).
16. Boyle, K. C. et al. Mechanisms of light-induced deformations in photoreceptors. *Biophys. J.* **119**, 1481–1488 (2020).
17. Bosse, B. et al. In vivo photovoltaic performance of a silicon nanowire photodiode-based retinal prosthesis. *Investig. Ophthalmol. Vis. Sci.* **59**, 5885–5892 (2018).
18. Karatum, O., Kaleli, H. N., Eren, G. O., Sahin, A. & Nizamoglu, S. Electrical stimulation of neurons with quantum dots via near-infrared light. *ACS Nano* **16**, 8233–8243 (2022).
19. Han, M., Karatum, O. & Nizamoglu, S. Optoelectronic neural interfaces based on quantum dots. *ACS Appl. Mater. Interfaces* **14**, 20468–20490 (2022).
20. Vanalakar, S. et al. Fabrication of Cu₂SnS₃ thin film solar cells using pulsed laser deposition technique. *Sol. Energy Mater. Sol. Cells* **138**, 1–8 (2015).
21. Vanalakar, S. et al. Non-vacuum mechanochemical route to the synthesis of Cu₂SnS₃ nano-ink for solar cell applications. *Acta Mater.* **85**, 314–321 (2015).
22. Kamble, A. et al. Monodispersed wurtzite Cu₂SnS₃ nanocrystals by phosphine and oleylamine free facile heat-up technique. *CrystEngComm* **18**, 2885–2893 (2016).
23. Jathar, S. B. et al. Ternary Cu₂SnS₃: synthesis, structure, photoelectrochemical activity, and heterojunction band offset and alignment. *Chem. Mater.* **33**, 1983–1993 (2021).
24. Palanker, D., Glowacki, E. D. & Ghezzi, D. Questions about the role of P3HT nanoparticles in retinal stimulation. *Nat. Nanotechnol.* **16**, 1330–1332 (2021).
25. Zhang, L., Zhu, J. & Li, K. Peroxidase activity based on Cu₂SnS₃ quantum dots for the degradation and visual detection of zearalenone. *Mater. Today Commun.* **35**, 105871 (2023).
26. Fernandes, P., Salomé, P. & Da Cunha, A. Study of polycrystalline Cu₂ZnSnS₄ films by Raman scattering. *J. Alloy. Compd.* **509**, 7600–7606 (2011).
27. Rand, D. et al. Direct electrical neurostimulation with organic pigment photocapacitors. *Adv. Mater.* **30**, 1707292 (2018).
28. Martino, N., Ghezzi, D., Benfenati, F., Lanzani, G. & Antognazza, M. R. Organic semiconductors for artificial vision. *J. Mater. Chem. B* **1**, 3768–3780 (2013).
29. Wang, C., Zhang, X. & Hu, W. Organic photodiodes and phototransistors toward infrared detection: materials, devices, and applications. *Chem. Soc. Rev.* **49**, 653–670 (2020).
30. Zheng, Q. & Shao, H. Correlation between redox species adsorption and electron transfer kinetics of mildly oxidized graphene: a chronocoulometry and SECM study. *Electrochem. Commun.* **103**, 83–87 (2019).
31. Krishnaveni, P. & Ganesh, V. Electron transfer studies of a conventional redox probe in human sweat and saliva bio-mimicking conditions. *Sci. Rep.* **11**, 7663 (2021).
32. Bao, L. et al. Artificial shape perception retina network based on tunable memristive neurons. *Sci. Rep.* **8**, 13727 (2018).
33. van Bavel, S. S., Loos, J., Baerenklau, M. & Hoppe, H. P3HT/PCBM bulk heterojunction solar cells: impact of blend composition and 3D morphology on device performance. *Adv. Funct. Mater.* **20**, 1458–1463 (2010).
34. Jia, H., Cheng, S., Zhang, H., Yu, J. & Lai, Y. Band alignment at the Cu₂SnS₃/In₂S₃ interface measured by X-ray photoemission spectroscopy. *Appl. Surf. Sci.* **353**, 414–418 (2015).
35. Srivastava, S. B. et al. Bulk-heterojunction photocapacitors with high open-circuit voltage for low light intensity photostimulation of neurons. *J. Mater. Chem. C* **9**, 1755–1763 (2021).
36. Srivastava, S. B., Srivastava, S. K. & Singh, S. P. Molecular-shape-induced efficiency enhancement in PC61BM and PC71BM based ternary blend organic solar cells. *J. Phys. Chem. C* **121**, 17104–17111 (2017).
37. Dias, S., Kumawat, K., Biswas, S. & Krupanidhi, S. B. Solvothermal synthesis of Cu₂SnS₃ quantum dots and their application in near-infrared photodetectors. *Inorg. Chem.* **56**, 2198–2203 (2017).
38. Mosconi, E. et al. Surface polarization drives photoinduced charge separation at the P3HT/water interface. *ACS Energy Lett.* **1**, 454–463 (2016).
39. Rose, T. & Robblee, L. Electrical stimulation with Pt electrodes. VIII. Electrochemically safe charge injection limits with 0.2 ms pulses (neuronal application). *IEEE Trans. Biomed. Eng.* **37**, 1118–1120 (1990).
40. Kuzum, D. et al. Transparent and flexible low noise graphene electrodes for simultaneous electrophysiology and neuroimaging. *Nat. Commun.* **5**, 5259 (2014).
41. Deng, Q. et al. Exploring optoelectronic properties and mechanisms of layered ferroelectric K₄Nb₆O₁₇ nanocrystalline films and nanolaminas. *Sci. Rep.* **7**, 1883 (2017).
42. Patil, S., Bhosale, A., Kundale, S., Dongale, T. & Vanalakar, S. Enhancing capacitance performance of functional group assisted carbon quantum dots derived from turmeric plant waste. *Carbon Trends* **15**, 100370 (2024).
43. Merrill, D. R., Bikson, M. & Jefferys, J. G. Electrical stimulation of excitable tissue: design of efficacious and safe protocols. *J. Neurosci. Methods* **141**, 171–198 (2005).
44. Jakešová, M. et al. Optoelectronic control of single cells using organic photocapacitors. *Sci. Adv.* **5**, eaav5265 (2019).
45. Kaya, L. et al. MnO₂ nanoflower integrated optoelectronic biointerfaces for photostimulation of neurons. *Adv. Sci.* **10**, 2301854 (2023).
46. Cogan, S. F. Neural stimulation and recording electrodes. *Annu. Rev. Biomed. Eng.* **10**, 275–309 (2008).
47. McCreery, D. B., Agnew, W. F. & Bullara, L. A. The effects of prolonged intracortical microstimulation on the excitability of pyramidal tract neurons in the cat. *Ann. Biomed. Eng.* **30**, 107–119 (2002).
48. Pulikodan, V. K. et al. Origin of anomalous transient photocurrent in solution-processed WS₂ nanosheet-based self-powered photodetectors. *ACS Appl. Nano Mater.* **7**, 8007–8021 (2024).
49. Le Formal, F., Sivula, K. & Grätzel, M. The transient photocurrent and photovoltage behavior of a hematite photoanode under working conditions and the influence of surface treatments. *J. Phys. Chem. C* **116**, 26707–26720 (2012).
50. Đerek, V., Rand, D., Migliaccio, L., Hanein, Y. & Glowacki, E. D. Untangling photofaradaic and photocapacitive effects in organic

- optoelectronic stimulation devices. *Front. Bioeng. Biotechnol.* **8**, 284 (2020).
51. Melikov, R. et al. Plasmon-coupled photocapacitor neuromodulators. *ACS Appl. Mater. Interfaces* **12**, 35940–35949 (2020).
52. Srivastava, S. B. et al. Band alignment engineers faradaic and capacitive photostimulation of neurons without surface modification. *Phys. Rev. Appl.* **11**, 044012 (2019).
53. Aria, M. M. *Electrophysiology Measurements for Studying Neural Interfaces* (Academic Press, 2020).
54. Hodgkin, A. L. & Huxley, A. F. A quantitative description of membrane current and its application to conduction and excitation in nerve. *J. Physiol.* **117**, 500 (1952).
55. Mervin, L. H. et al. Understanding cytotoxicity and cytostaticity in a high-throughput screening collection. *ACS Chem. Biol.* **11**, 3007–3023 (2016).
56. Mohammadiaria, M. Photoelectrical control of apoptosis and autophagy. *Biophys. Rep.* **6**, 100241 (2026).
57. Robinson, A. J. et al. Toward Hijacking Bioelectricity in Cancer to Develop New Bioelectronic Medicine. *Adv. Ther.* **4**, 2000248 (2021).

Acknowledgements

This work is supported by the Scientific and Technological Research Council of Türkiye (TÜBİTAK) and the European Commission Co-Funded Scheme through The Marie Curie Action Cofund of the 7th Framework Programme (FP7) under Project 121C046 and Priority Research Centers Program through the National Research Foundation of Korea (NRF) funded by the Ministry of Education, Science and Technology (2018R1A6A1A03024334). SAV is thankful to Dr. Sedat Nizamoglu of the Innovative Devices and Interfaces Laboratory (IDEALAB), Koç University, Istanbul (Türkiye), for providing the research facilities to perform the LED-associated experiments. The authors are thankful to Humeyra Nur Kaleli of the Research Centre of Translational Medicine at Koç University, Istanbul (Türkiye), for providing the biocompatibility testing experiments. The S.B.S. thanks the support provided by the Department of Ophthalmology at Henry Ford Health.

Author contributions

S.A.V. and S.B.S. gave the idea, supervised, and wrote the main manuscript. M.H.Q. did the calcium imaging and wrote the corresponding text. M.M. and S.B.S. did the theoretical simulations. M.M. prepared Figure 4. S.S.V. contributed to the fabrication of the device. S.A.V. and S.B.S. did the

electrochemical measurement and analysis. J.H.K. supervised, contributed to the study and assisted in writing the manuscript. All authors reviewed the manuscript.

Competing interests

The authors declare no competing interests.

Additional information

Supplementary information The online version contains supplementary material available at <https://doi.org/10.1038/s41528-026-00531-x>.

Correspondence and requests for materials should be addressed to Sharadrao A. Vanalakar, Mohammad H. Qureshi, Jin H. Kim or Shashi B. Srivastava.

Reprints and permissions information is available at <http://www.nature.com/reprints>

Publisher's note Springer Nature remains neutral with regard to jurisdictional claims in published maps and institutional affiliations.

Open Access This article is licensed under a Creative Commons Attribution-NonCommercial-NoDerivatives 4.0 International License, which permits any non-commercial use, sharing, distribution and reproduction in any medium or format, as long as you give appropriate credit to the original author(s) and the source, provide a link to the Creative Commons licence, and indicate if you modified the licensed material. You do not have permission under this licence to share adapted material derived from this article or parts of it. The images or other third party material in this article are included in the article's Creative Commons licence, unless indicated otherwise in a credit line to the material. If material is not included in the article's Creative Commons licence and your intended use is not permitted by statutory regulation or exceeds the permitted use, you will need to obtain permission directly from the copyright holder. To view a copy of this licence, visit <http://creativecommons.org/licenses/by-nc-nd/4.0/>.

© The Author(s) 2026